Multiphase Science and Technology, 32(2):137–154 (2020)

SURFACE WETTING IN MULTIPHASE PIPE-FLOW

Jakob R. Bentzon,[1,*] Attila Vural,[1] Karen L. Feilberg,[2] & Jens H. Walther[3,4]

[1]*Department of Mechanical Engineering, Technical University of Denmark, Kgs. Lyngby, Denmark*

[2]*The Danish Hydrocarbon Research and Technology Centre, Technical University of Denmark, Kgs. Lyngby, Denmark*

[3]*Department of Mechanical Engineering, Technical University of Denmark, Kgs. Lyngby, Denmark*

[4]*Computational Science and Engineering Laboratory, ETH, Zürich, CH-8092, Switzerland*

*Address all correspondence to: Jakob R. Bentzon, Department of Mechanical Engineering, Technical University of Denmark, Kgs. Lyngby, 2800, Denmark, E-mail: jroben@mek.dtu.dk

Original Manuscript Submitted: 7/15/2019; Final Draft Received: 2/17/2020

The present study examines the quantity of surface wetting in a two-phase oil and water pipe flow. The study is performed by employing an Eulerian-Eulerian computational fluid dynamics model using the S-gamma droplet size distribution model within STAR–CCM+. In the North Sea, production of oil and gas, water-phase surface processes such as scale and corrosion account for 40–50% of operating expenses. The objective of the study is to investigate best practices for the prediction of phase distribution aimed at evaluating the degree of the wall in contact with the water phase (water-wetting). The model is validated by performing detailed numerical simulations corresponding to the experimental studies by Kumara, Halvorsen, and Melaaen (Meas. Sci. Technol., vol. **20***, p. 114004, 2009). The comparison yields good agreement with the observed measurements with slight deviations in the predicted dispersion rate but accurate prediction of the liquid holdup. Comparison of droplet sizes to those observed in experiments by Elseth (PhD, Telemark University College, 2001) indicates that tuning of the S-gamma model is necessary to provide accurate droplet size predictions. The surface wetting is then evaluated with its interdependence with liquid holdup and dispersion rate. Increase in the dispersion with a decrease in the Richardson number is observed in agreement with stability analysis of the Kelvin-Helmholtz instability.*

KEY WORDS: *multiphase, CFD, Euler-Euler, water-wetting, liquid holdup, STAR–CCM+, S-gamma, droplet size, oil, surface wetting*

1. INTRODUCTION

Flow assurance is a major challenge in the oil and gas industries and amounts to 40–50% of the total operating expenses in many wells due to costly mechanical and chemical intervention. The presence of hard and soft scales (e.g., $CaCO_3$, $BaSO_4$, $FeCO_3$, FeS) might lead to loss of

production due to scale build up and enhanced corrosion rates due to galvanic effects and fouling of equipment, which can lower the production rates and ultimately render oil-wells unrecoverable. Consequently, it is of major importance to understand the mechanisms and the rates of corrosion and scale deposition under hydrodynamic conditions and realistic flow in the production wells.

Understanding the proportion of wall in contact with the water phase, a property known as water-wetting is crucial for the development and analysis of mitigation measures. The flow regime varies from stratified to fully dispersed throughout the well; therefore, a fully qualified model should capture the physics of both flow regimes. The application of the volume-of-fluid (VOF) approach to model dispersion of the phases requires interface resolution of the droplets in the flow (Hirt and Nichols, 1981). The average droplet sizes in fully dispersed flows are estimated to be on the order of 1 mm based on the maximum diameter observed in experiments by Elseth (2001). This makes the use of the VOF model infeasible for the dispersed flow regime. In contrast, the Eulerian-Eulerian two-equation approach allows for subgrid, droplet-dispersion modeling through empirical closure laws and is used throughout this work. This method has been used successfully for a number of liquid-liquid and liquid-gas flows (Prosperetti and Tryggvason, 2007).

Attempts to simulate the study by Kumara et al. (2008) using the VOF approach shows good prediction of the velocity profiles and pressures but does not describe the dispersion of the phases. A Eulerian-Eulerian approach using droplet sizes determined from the correlations by Brauner (2001) has been studied by Pouraria et al. (2016) to replicate the results from Elseth (2001) and has achieved fairly good agreement. The accuracy of the Eulerian-Eulerian approach depends on the models for determining the transfer of momentum between the phases. Typically, this included drag, lift, surface tension, virtual mass, and surface contact forces. These models depend on an estimate of the droplet size. Modeling attempts with a constant droplet size have proven to have limited success in predicting dispersion adequately. Consequently, the present study employs the S-gamma droplet size distribution model described by Lo and Zhang (2009).

From the aforementioned work, it is clear that the Eulerian-Eulerian model has good potential as a tool for studies of two-phase flow in oil wells. Thus, a thorough study to validate the model and its parameters is essential for further research. The objective of the present study is to validate and optimize the numerical procedure for two-phase oil and water pipe flows against the experiments from Elseth (2001) and Kumara et al. (2009). The resulting distribution of the phases is compared to gamma densitometry measurements of cross-sectional phase distributions by Kumara et al. (2009). Similarly, the droplet sizes obtained by the S-gamma droplet size distribution model is compared to droplet sizes obtained by visual inspection in the study by Elseth (2001).

To analyze surface wetting, the consequence of liquid holdup (i.e., flow properties causing one fluid to move slower than the other and thereby increasing its share of cross-sectional area in the pipe) is analyzed. Additionally, the rate of dispersion affects how much of each phase is in contact with the wall. Using a validated model, these two phenomena can be analyzed for different flow properties.

2. METHODOLOGY

A numerical computational fluid dynamics (CFD) model is set up in the STAR–CCM+ version 13.04 to investigate the best modeling settings for replicating the experimental study by Elseth (2001) and Kumara et al. (2009). The test rig illustrated in Fig. 1 consists of a pipe section with

FIG. 1: Illustration of the experimental model described in Elseth (2001)

diameter $D = 0.0563$ m and length 12 m (213 diameters), followed by a test section where time-averaged gamma densitometry measurements were taken across a set of cords in the horizontal direction. The pipe section is preceded by a Y-junction from which oil and water flows into each inlet. The flow is controlled by the flow rate of each phase k ($k \in w, o$, where o denotes oil and w denotes water) and is reported in terms of mean velocity $U = (\dot{V}_w + \dot{V}_o)/(D^2\pi/4)$ and water-cut $\psi = \dot{V}_w/(\dot{V}_w + \dot{V}_o)$, where $\dot{V}_w$ and $\dot{V}_o$ are the volumetric flow rates of water and oil. The CFD model assumes symmetry in the plane spanned by the axial direction of the pipe and the gravitational direction.

2.1 Governing Equations

The numerical simulations are based on the Eulerian-Eulerian two-fluid approach. This treats both phases as a continuous phase, each with its own velocity field $\mathbf{u}_k$ but with a shared pressure field p (Ishii and Hibiki, 2006). The fluids are considered isothermal, immiscible, and incompressible. Hence, only mass and momentum conservation is considered. Both equations are averaged with a Reynolds decomposition to obtain a solution for the mean flow. This gives a set of volume-fraction-Averaged Reynolds averaged Navier-Stokes (RANS) equations for each of the two phases

$$\frac{\partial \alpha_k}{\partial t} + \nabla \cdot (\alpha_k \mathbf{u}_k) = 0 \tag{1}$$

$$\frac{\partial \alpha_k \rho_k \mathbf{u}_k}{\partial t} + \nabla \cdot (\rho_k \alpha_k \mathbf{u}_k \mathbf{u}_k) = -\alpha_k \nabla p + \alpha_k \rho_k \mathbf{g} + \nabla \cdot \left\{ \alpha_k \mu_{k,\text{eff}} \left[\nabla \mathbf{u}_k + (\nabla \mathbf{u}_k)^T \right] \right\} + \mathbf{M}_k \tag{2}$$

where ρ_k and α_k are the density and volume fraction of the kth phase, $\mathbf{g}$ is the gravitational vector set to $\mathbf{g} = (-9.82 \sin\beta, -9.82 \cos\beta, 0)$ m/s^2, where β is the inclination angle of the pipe. $\mu_{k,\text{eff}} = \mu_k + \mu_{k,t}$ is the effective dynamic viscosity composed of the dynamic viscosity of the fluid (μ_k) and the turbulent viscosity ($\mu_{k,t}$) from the RANS decomposition, cf. Ishii and Hibiki (2006). A realizable k-ϵ model is used to determine the turbulent viscosity (Shih et al., 1995). All model parameters are left as per STAR–CCM+ defaults. The term $\mathbf{M}_k$ corresponds to the exchange of momentum between the two phases. The interfacial momentum transfer forces are subdivided into drag ($\mathbf{M}_{D,k}$), lift ($\mathbf{M}_{L,k}$), turbulent dispersion ($\mathbf{M}_{T,k}$), virtual mass ($\mathbf{M}_{V,k}$), and surface tension ($\mathbf{M}_{S,k}$):

$$\mathbf{M}_k = \mathbf{M}_{D,k} + \mathbf{M}_{L,k} + \mathbf{M}_{T,k} + \mathbf{M}_{V,k} + \mathbf{M}_{S,k} \tag{3}$$

where each of the interfacial forces are modeled using empirical closure laws.

2.2 Interfacial Forces

The interfacial drag, lift, turbulence dispersion, and virtual mass forces (generically denoted $M_{F,k}$) are modeled in three different regimes based on the volume fraction of water α_w. The

two primary regimes are namely, the $D_{w/o}$ (dispersed water-in-oil) for $\alpha_w < 0.3$, the $D_{o/w}$ (dispersed oil-in-water) for $\alpha_w > 0.7$, cf. Cerne et al. (2001). In the intermediate range, a volume fraction averaged force is used. Between the two dispersed regions and the intermediate region, a blending zone of width 0.1 volume fraction is used.

$$\mathbf{M}_{F,k} = \begin{cases} \mathbf{F}_{F,w/o} & \alpha_w < 0.3 \\ \mathbf{F}_{F,o/w} & \alpha_w > 0.7 \\ f_w \mathbf{F}_{F,o/w} + f_o \mathbf{F}_{F,w/o} & \alpha_w \in [0.3, 0.7] \end{cases} \tag{4}$$

where the blending function f_k is given by

$$f_k = \begin{cases} \dfrac{0.4}{0.1}(\alpha_k - 0.3) & \alpha_k \in [0.3, 0.4] \\ \alpha_k & \alpha_k \in [0.4, 0.6] \\ 0.6 + \dfrac{0.4}{0.1}(\alpha_k - 0.6) & \alpha_k \in [0.6, 0.7] \end{cases} \tag{5}$$

The drag force $\mathbf{F}_{D,d/c}$ of a dispersed droplet of phase d in the continuous phase c is computed as follows:

$$\mathbf{F}_{D,d/c} = \frac{1}{2}\rho_p C_D |\mathbf{u}_d - \mathbf{u}_c|(\mathbf{u}_d - \mathbf{u}_c)\frac{A_{CD}}{4} \tag{6}$$

where A_{CD} is the mean interfacial area obtained from the droplet size distribution described in Section 2.3.

The drag coefficient in the $D_{w/o}$ and $D_{o/w}$ regimes are computed using the Schiller-Naumann model (Schiller and Naumann, 1933):

$$C_D = \begin{cases} \dfrac{24(1 + 0.15\mathrm{Re}_D^{0.687})}{\mathrm{Re}_D} & \mathrm{Re}_D \leq 1000 \\ 0.44 & \mathrm{Re}_D > 1000 \end{cases} \tag{7}$$

where the Reynolds number of the droplets (Re_D) is defined as:

$$\mathrm{Re}_D = \frac{\rho_c |\mathbf{u}_d - \mathbf{u}_c| d_{32}}{\mu_c} \tag{8}$$

where d refers to the dispersed phase (water for $D_{w/o}$ and oil for $D_{o/w}$) and c the continuous phase, d_{32} is the Sauter mean diameter of the droplets described in Schümann et al. (2015) and Lo and Zhang (2009).

As a dispersed droplet moves relative to a shear flow, it will experience a lift force perpendicular to the relative velocity proportional to the curl of the continuous phase velocity (Auton et al., 1988).

$$\mathbf{F}_{L,d/c} = -C_L \rho_c \alpha_d (\mathbf{u}_d - \mathbf{u}_c) \times (\nabla \times \mathbf{u}_c) \tag{9}$$

where the lift force coefficient C_L is set to a constant of 0.25, cf. Lance and Bataille (1991).

As a dispersed droplet accelerates relative to the continuous phase, the acceleration of a part of the continuous phase requires modeling of the added mass (Auton et al., 1988)

$$\mathbf{F}_{V,d/c} = C_{VM} \rho_c \alpha_d \mathbf{a}_{\text{rel}} \tag{10}$$

where C_{VM} is the coefficient of virtual mass derived from inviscid flow theory to 0.5 for a sphere (Lamb, 1932) and $\mathbf{a}_{\text{rel}}$ is the relative acceleration of the phases

$$\mathbf{a}_{\text{rel}} = \frac{D\mathbf{u}_d}{Dt} - \frac{D\mathbf{u}_c}{Dt} \tag{11}$$

When applying the Reynolds averaging to the drag term, the nonlinear term gives rise to an extra turbulent dispersion term. This can be modeled as a dispersion drag coefficient C_{TD} on a turbulent dispersion velocity $\mathbf{u}_{TD}$.

$$\mathbf{M}_T = C_{TD}\mathbf{u}_{TD} \tag{12}$$

The turbulent dispersion velocity has its origin in the phase and Reynolds averaging and is approximated through the Boussinesq closure to

$$\mathbf{u}_{TD} \approx -\frac{\mu_{c,t}}{\rho_c \sigma_\alpha}\left(\frac{\nabla\alpha_c}{\alpha_c} - \frac{\nabla\alpha_d}{\alpha_d}\right) \tag{13}$$

where α_c, α_d are the Reynolds-averaged volume fractions of the continuous and dispersed phase, σ_α is the a coefficient describing the ratio of turbulent dispersion of volume fraction to that of momentum and is set to unity in this work. The turbulent dynamic viscosity is obtained from the k-ϵ model.

The turbulent dispersion drag coefficient, C_{TD}, is defined from a Stokesian drag coefficient and linearized with the relative velocity of the two averaged phases

$$C_{TD} = \frac{A_{CD}}{8}\rho_c C_D |\mathbf{u}_c - \mathbf{u}_d| \tag{14}$$

The droplet drag coefficient C_D is modeled using a Schiller-Naumann drag coefficient described by Eq. (7). The determination of which phase is continuous and dispersed is handled similarly to the drag force by Eq. (4).

Surface tension forces arises directly in the interfaces between the fluids. The Eulerian-Eulerian two-fluid model does not explicitly track the interface between the phases. To account for surface tension in the physical interface on larger fluid structures, the continuum surface tension model proposed by Brackbill et al. (1992) and described for a Eulerian-Eulerian two-fluid by Strubelj et al. (2009) is used. The numerical procedure is to reconstruct the surface normal based on one (primary, e.g., water) of the phases $\mathbf{n}_p$ and curvature κ_p

$$\mathbf{n}_p = \frac{\nabla\alpha_p}{|\nabla\alpha_p|} \tag{15}$$

$$\kappa_p = -\nabla \cdot \mathbf{n}_p \tag{16}$$

On the basis of the curvature, the surface tension force at the interface becomes

$$\mathbf{F}_S = \sigma\kappa_p\nabla\alpha_p \tag{17}$$

where σ is the surface tension in units force per length. The force is split between the two phases by dividing the force in the momentum equations relative to the local volume fraction

$$\mathbf{F}_{S,k} = \alpha_k \mathbf{F}_S \tag{18}$$

To simulate the interaction of the interface at the wall, the wall wetting contact angle θ_w is implemented by defining the interface normal vector of the first computational cell as a transformation of the unit normal vector of the wall $\mathbf{n}_w$ and tangential vector $\mathbf{t}_w$

$$\mathbf{n}_{p,\text{wall}} = \mathbf{n}_w \cos\theta_w + \mathbf{t}_w \sin\theta_w \tag{19}$$

With limited fluid properties available for the given mixture of water and oil, the wetting angle θ_w is set to 41 deg based on measurements of deacidified deasphaltened crude oil on stainless steel surfaces in a pure water solution by dos Santos et al. (2006).

In order to accurately determine the volume fraction gradients at interfaces, an interface compressing scheme was suggested by Strubelj et al. (2009). The interface sharpening method technique described by Coste (2013) has been used to produce a sharp interface marker function from comparison of cell surface volume fractions. This marker function is used to adaptively shift between the interface compressing high resolution interface capturing (HRIC) scheme described by Muzaferija and Peric (1997) and the total variation diminishing (TVD) scheme to avoid artificially sharpening interfaces in naturally dispersed regions.

2.3 Droplet Size

A key to modeling the interfacial forces is the correct estimation of droplet sizes and area density. For this purpose, the present study employs the S-gamma statistical droplet size distribution model developed by Lo and Zhang (2009). The S-gamma model describes the particles through three moments S_γ, where $\gamma \in 0, 2, 3$. Numerically, the model solves for the second moment, S_2, which describes the interfacial area density, and optionally it can additionally solve for the zeroth moment, S_0, describing the particle number density. The third moment, S_3, describes the volume density of the droplets and is thus directly correlated to the volume fraction of the dispersed phase

$$S_{3,k} = \frac{6}{\pi}\alpha_k \tag{20}$$

In this study, only the second moment is used and modeled for both phases. This is computationally simpler but limited to model the Sauter mean diameter, d_{32}, but does not yield the variance of the droplet size distribution. The second moment is formulated as the integral over the droplet size distribution of the square of the diameter and hence represents the droplet mean interfacial area (A_{CD}) divided by π

$$S_2 = \int d_p^2 n(d_p) d(d_p) = \frac{A_{CD}}{\pi} \tag{21}$$

By assuming spherical droplets, the Sauter mean diameter can be calculated as follows:

$$d_{32,k} = \frac{S_{3,k}}{S_{2,k}} \tag{22}$$

The S_γ moments are modeled as convective scalars tracked with a scalar transport equation

$$\frac{\partial S_{\gamma,k}}{\partial t} + \nabla \cdot (S_{\gamma,k}\mathbf{u}_k) = s_{br,k} + s_{cl,k} \tag{23}$$

The source terms $s_{br,k}$ and $s_{cl,k}$ model breakup and coalescence through empirical models described in Lo and Zhang (2009). The critical Weber number used in these models is set to 0.5 for both phases, cf. Hill (1998).

To ensure a stable simulation, the droplet size is initially modeled empirically. Here, a model by Brauner (2001) is employed to estimate the maximum droplet diameter

$$\frac{d_{\max}}{D} = 7.61 \mathrm{We}_c^{-0.6} \mathrm{Re}_c^{0.08} \left(\frac{\alpha_d}{\alpha_c} \right)^{0.6} \left(1 + \frac{\rho_d}{\rho_c} \frac{\alpha_d}{\alpha_c} \right)^{-0.4} \tag{24}$$

where We_c and Re_c are the Weber and Reynolds number of the continuous phase. The Reynolds number is the ratio of inertial to viscous forces; whereas, the Weber number is the ratio of inertial forces to surface tension

$$\mathrm{Re} = \frac{\rho U D}{\mu} \tag{25}$$

$$\mathrm{We} = \frac{\rho U^2 D}{\sigma} \tag{26}$$

Empirical studies and observations from experiments typically report the maximum diameter $d_{\max}$. The ratio between the maximum observed diameter and the Sauter mean diameter has been reported from experimental studies by Angeli and Hewitt (2000) to

$$d_{32} = 0.48 \, d_{\max} \tag{27}$$

2.4 Flow Conditions

The physics describing the model shows the complex array of parameters affecting the flow. The parameters of the validation are described in Table 1. To simplify the variation study, flow parameters are described in terms of nondimensionalized numbers. A variety of different dimensionless quantities can be considered. In this study, the Atwood and Richardson numbers are studied to account for Rayleigh-Taylor and the Kelvin-Helmholtz instabilities. These two instabilities are considered relevant for the stability of the interface and thus the transition between flow patterns. Aside from the aforementioned, the more typical fluid dynamics characteristics are described through the Reynolds and Weber numbers from Eqs. (25) and (26) as well as the Froude number (Fr), which characterizes the ratio of gravity to inertial forces

$$\mathrm{Fr} = \frac{U}{\sqrt{g_y D}} \tag{28}$$

TABLE 1: Parameters from experimental reference study (Elseth, 2001; Kumara et al., 2009) and wetting contact angle estimated from dos Santos et al. (2006)

Parameter	Value
Pipe diameter, D	0.0563 m
Oil density, ρ_o	790 kg/m^3
Oil viscosity, μ_o	0.00164 Pa s
Water density, ρ_w	1000 kg/m^3
Water viscosity, μ_w	0.00102 Pa s
Surface tension, σ	0.043 N/m
Wetting contact angle, θ_w	41°

The Atwood number describes the ratio of the difference in density to the average density and is often arises as a factor for instabilities in two-phase flows. The Atwood number arises analytically from analysis of the Rayleigh-Taylor instability (Glimm et al., 2001; Taylor, 1950)

$$\mathrm{A} = \frac{\rho_w - \rho_o}{\rho_w + \rho_o} \tag{29}$$

The Richardson number describes the ratio of buoyancy forces to shear forces. It arises from stability analysis of the Taylor-Goldstein equation as the criterion for stability of the Kelvin-Helmholtz instability. This describes the stability of a shear flow with a density gradient (Goldstein, 1931; Taylor, 1931). Locally for a pure shear flow in an inviscid incompressible fluid with a uniform density gradient, it is defined as follows:

$$\mathrm{Ri} = \frac{-g_y}{\rho} \frac{\partial \rho / \partial y}{|\partial u_x / \partial y|^2} \tag{30}$$

For an interface with a nonuniform density or velocity gradient, an average global cross-sectional Richardson number is approximated as the ratio of the Atwood number to the square of the Froude number

$$\mathrm{Ri} = \frac{\rho_w - \rho_o}{\rho} \frac{g_y D}{U^2} \approx \frac{2A}{\mathrm{Fr}^2} \tag{31}$$

For inviscid stratified pure shear flow, stability analysis shows that all wavelengths are stable for $\mathrm{Ri} > 0.25$ (Hazel, 1972). For the viscous flow, viscosity acts as a damping factor when Re is low but has more complex effects in higher Reynolds numbers, where the surface tension further dampens the instability of the interface (Drazin and Reid, 2004; Turner, 1973).

The flow conditions of the present study are of a more complex nature with phase distribution and boundaries giving lead to nonuniform density and velocity gradients. Hence, the criterion of Ri is not well-defined. However, the expected trend is that the stability of the interface is stabilized with increased Atwood number or decreased Froude number.

2.5 Numerical Model

The domain boundary is divided into two inlets, a symmetry plane, a wall, and an outlet as illustrated in Fig. 2. The inlets are given Dirichlet boundary conditions with prescribed phase-velocities $\mathbf{u}_k$, volume fraction α_k, droplet sizes $d_{32,k}$, turbulent intensity I_k, and viscosity ratio $\mu_{k,t}/\mu_k$. The pressure is extrapolated from the domain through reconstruction gradients. The turbulent intensity is set to 0.01, and the viscosity ratio to 10 as per STAR–CCM+ defaults. Variation of inlet turbulence has been tested with little effect on the downstream results. The inlet droplet Sauter mean diameter is defined with a mean and variance of both $0.7D/2$.

The outlet is modeled by specifying the pressure to the hydraulic pressure based on the flow-rate averaged density using a Dirichlet condition. Other flow variables are extrapolated.

Symmetry in the plane spanned by the gravitational vector and axial direction of the pipe is exploited by a symmetry boundary condition (homogeneous Dirichlet on the normal component of the flow and homogeneous Neumann condition on the normal derivatives of all other equation variables).

The walls are modeled as no-slip walls with homogeneous Dirichlet conditions on the velocity field. The turbulence is modeled using a high y^+ wall treatment model because the wall boundary layer is not sought to be resolved (Shih et al., 1995).

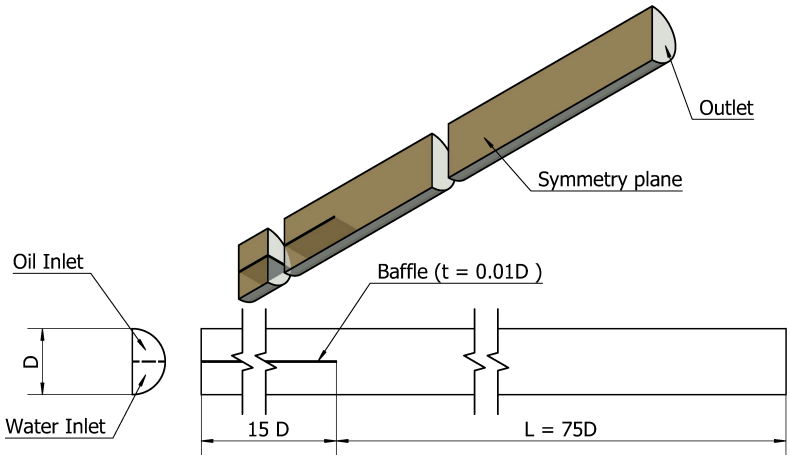

FIG. 2: Illustration of the computational domain. The length of $L = 75D$ is established by a pipe-length study described in Section 2.

The procedure of obtaining a numerical solution to the two-fluid model is split into three steps for the sake of numerical stability and convergence. Initially, a steady-state version of Eqs. (1) and (2) is solved by setting the time derivatives to zero. This has proven numerically unstable along with the droplet size distribution model and is instead carried out with a static constant droplet size determined by Eq. (24). The steady-state analysis is run for 1000 iterations. Subsequently, the simulation is switched to a transient analysis. Here, the S-gamma droplet size distribution is solved passively, i.e., without coupling the resulting droplet size to the terms for the momentum equation. This second step is solved with a Courant number of 5 and 40 inner iterations for a physical time of $tU/L = 0.7$. Finally, the droplet sizes used in the momentum equation is coupled to the S-gamma model and solved for another $tU/L = 0.75$ of physical time with a Courant number of 0.1 and a time-step convergence tolerance of 10^{-6} on all equation residuals.

The domain is presented in a Cartesian coordinate system with its origin at the mixing point of the incoming flows, the x-axis following the axial direction of the pipe, the z-axis horizontal in the gravitational field, with the y-axis following the pipe, aligned with gravity for the horizontal pipe. The computational domain is discretized by a rectangular trimmer mesh-grid, with cells in the axial direction of the pipe twice as long as in the radial. The grid sizing is controlled with a single nondimensional parameter $\hat{\delta}$. The cells located in the core of the domain is set to size $\delta = \hat{\delta}D$, where D is the diameter of the pipe. The traverse directions are refined to 0.25δ, and the boundaries are kept as quadratic with a maximum cell-to-cell stretch of 2. This gives a mesh as shown in Fig. 3.

The computational domain corresponding to the full experimental setup is computationally expensive to run. Therefore, a study is carried out to evaluate the necessary length of pipe needed for the phase distribution to have reached a constant state.

The validation is carried out by comparing the densitometry measurements presented by Kumara et al. (2009) to the postprocessed Reynolds-averaged numerical results. The postprocessing takes the cross-sectional volume fraction average in the z-direction to replicate the density line measurements of the densitometry. The data presented on a plot with the average volume fraction on the horizontal axis and the radius-normalized y-position on the vertical axis. From the

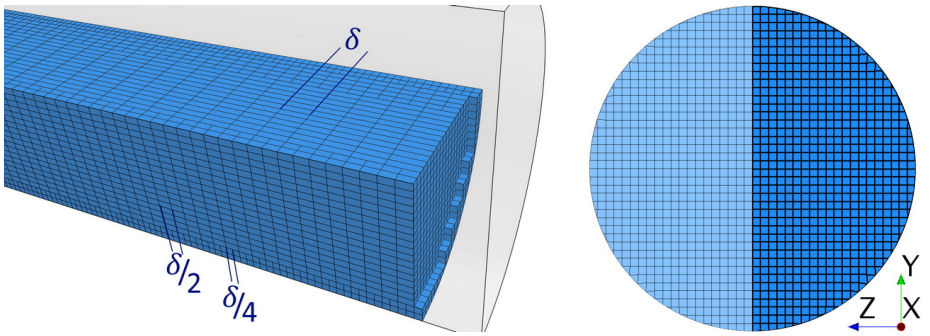

FIG. 3: (left) Illustration of the grid and picture extracted at the outlet of the pipe seen from the symmetry plane with a section cut out to reveal the interior of the grid domain. (right) Cross-sectional mesh (with opaque symmetry).

phase distributions, the level of dispersion and liquid holdup can be evaluated from Eq. (32). An example of such a cross-sectional volume fraction density plot can be seen in Fig. 4.

In a horizontal steady flow, a simple force consideration on the two fluids is employed in the x direction; each phase has a pressure gradient, viscous forces, and interfacial forces acting on it. The interfacial forces exerted are Newton's third law pairs. Given a fixed pressure gradient, the location of the interface is controlled by a force balance of the viscous and pressure gradient. For identical viscosities, the solution would tend to equal the inflow ratio such that the area integral of the volume fraction of water (α_w) over a cross section would equal the water-cut. As the viscosities differ, the interface moves and one phase moves slower relative to the other. This difference in velocity gives rise to liquid holdup, i.e., the phase volume ratio in the pipe of each phase is not equal to the water-cut. With the higher viscosity of the oil, a higher holdup of oil is expected. As the pipe is inclined (with the flow moving upward), gravity acts stronger on

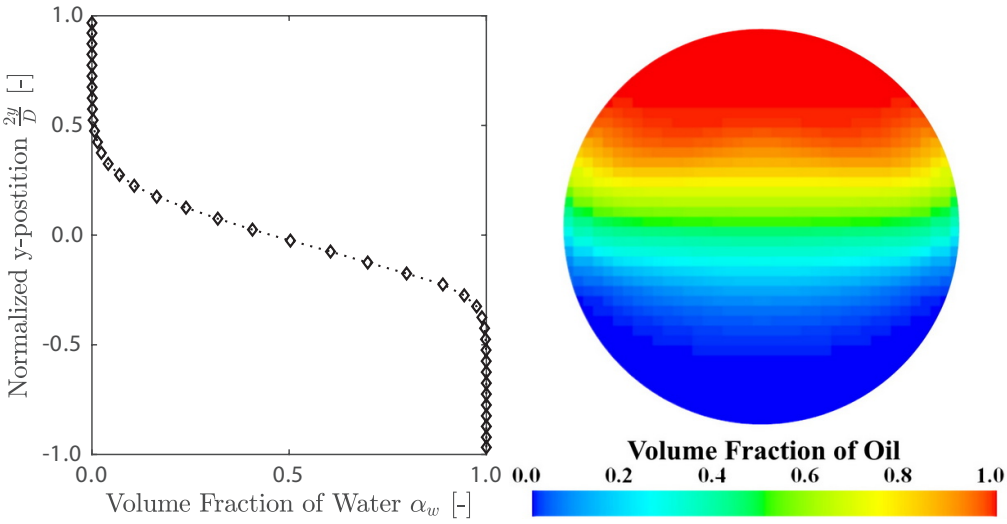

FIG. 4: (left) Postprocessing illustration of cross-sectional volume fraction density and (right) the corresponding phase distribution

the denser fluid and higher holdup of water is expected. The holdup of water increases water-wetting in the pipe and thus increases the risk of exposing the surface to corrosion and scale formation. On the phase distribution profiles, liquid holdup is indicated by the area under the curve differing from the water-cut. The rate of dispersion is indicated by the slope of the curve. The liquid holdup of water, Z_w, is postprocessed as the volume integral of the volume fraction of water divided by the total volume V_T in a five diameter long section of the pipe. A volume integral is used to average the cross-sectional area based liquid holdup smoothing out small variations in the axial direction of the pipe

$$Z_w = \frac{1}{V_T} \int_{V_T} \alpha_w dV \tag{32}$$

The numerical model implemented solves for averaged flow quantities due to the Reynolds averaging as well as the Eulerian description of the phase distribution in each computational cell. Consequently, an assumption is taken to provide a description of the wetting of the walls. In this study, the water-wetting of the wall, W_w, is assumed equal to the surface integral of the extrapolated water volume fraction from the adjacent cells, $\alpha_{w,\text{wall}}$ divided by the total area of the wall A_{wall}:

$$W_w = \frac{1}{\text{A}_{\text{wall}}} \int_{\text{A}_{\text{wall}}} \alpha_{w,\text{wall}} d\text{A} \tag{33}$$

This assumes the wetting to be independent on the expected underlying flow pattern (e.g., water droplets dispersed in oil).

3. RESULTS AND DISCUSSION

This section describes the validation of the present CFD model with experimental data from Kumara et al. (2009), and an analysis based on the validated model with purpose of understanding how water-wetting of the surface is controlled by flow properties. The flow cases used for validation are listed in Table 2.

3.1 Pipe Length Independence Study

A study of the pipe length for the CFD model required to converge to a constant phase distribution profile is performed to reduce the number of computational cells used in the subsequent convergence and variation studies. The results from Kumara et al. (2009) are used as a reference.

TABLE 2: Input condition for the different case studies in the validation analysis. U is the mean velocity, ψ is the water cut, Re the Reynolds number, Ri is the Richardson number, Fr is the Froude number, We is the Weber number, and β the inclination angle. The Atwood number is constant ($\text{A} = 0.12$) as no variations in fluid properties have been tested in the experiments referenced

β (deg)	U (m/s)	ψ (%)	Re	Ri	Fr	We
0	1.0	50	38,000	0.13	1.3	1200
0	1.5	50	57,000	0.06	2.0	2600
0	1.5	75	68,000	0.06	2.0	2800
5	1.0	50	38,000	0.13	1.3	1200

The study is performed on a medium-fine mesh of grid size $\hat{\delta} = 0.15$ on a pipe of total length of $265D$. An extract of the results at different x-positions is shown in Fig. 5.

It is observed that while the results, using an intermediate grid size $\hat{\delta} = 0.15$, display some differences with the experimental, the profiles do converge from ~ 50 diameters downstream until approximately five diameters before the outlet where the profile evolves leading up to the boundary. In the remainder of this work, a pipe length of $75D$ is used with sampling at $x = 55D$.

Another study is performed for the necessary pipe length upstream from the mixing point in order for the velocity profile to develop (not shown). Here, a length of 15 diameters is concluded to be sufficient length preceding the mixing point. It is noted that wave in the interface occur in the earlier section of the pipe with a wavelength of approximately five to six diameters. The results are time-averaged over a timespan based on wave period assuming the wave travels with the mean flow velocity.

3.2 Mesh Convergence Study

A study of the spatial resolution is conducted on four cases for horizontal flows with a mean velocity of $U = 1.0$ and $U = 1.5$ m/s using water-cuts of $\psi = 50$ and $\psi = 75\%$ as well as upward inclined flows angled at $\beta = 0$ and $\beta = 5$ deg at $U = 1$ m/s mean velocity and $\psi = 50\%$ water-cut.

For the horizontal flow at $U = 1.0$ m/s with $\psi = 50\%$ water-cut, four mesh sizes are tested, $\hat{\delta} \in [0.4, 0.2, 0.1, 0.05]$. The results are shown in Fig. 6(a). It is seen that the y-position at which the first oil is observed converges toward the experimental observations; whereas, the gradient of the volume fraction converges toward a result with slightly overpredicted dispersion.

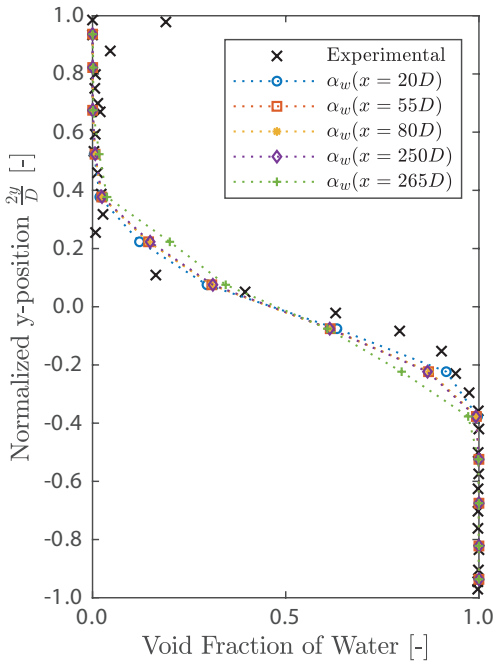

FIG. 5: Comparison of cross-sectional phase distribution at different x-positions. Horizontal flow, $U = 1.0$ m/s, $\psi = 50\%$. Experimental reference by Kumara et al. (2009).

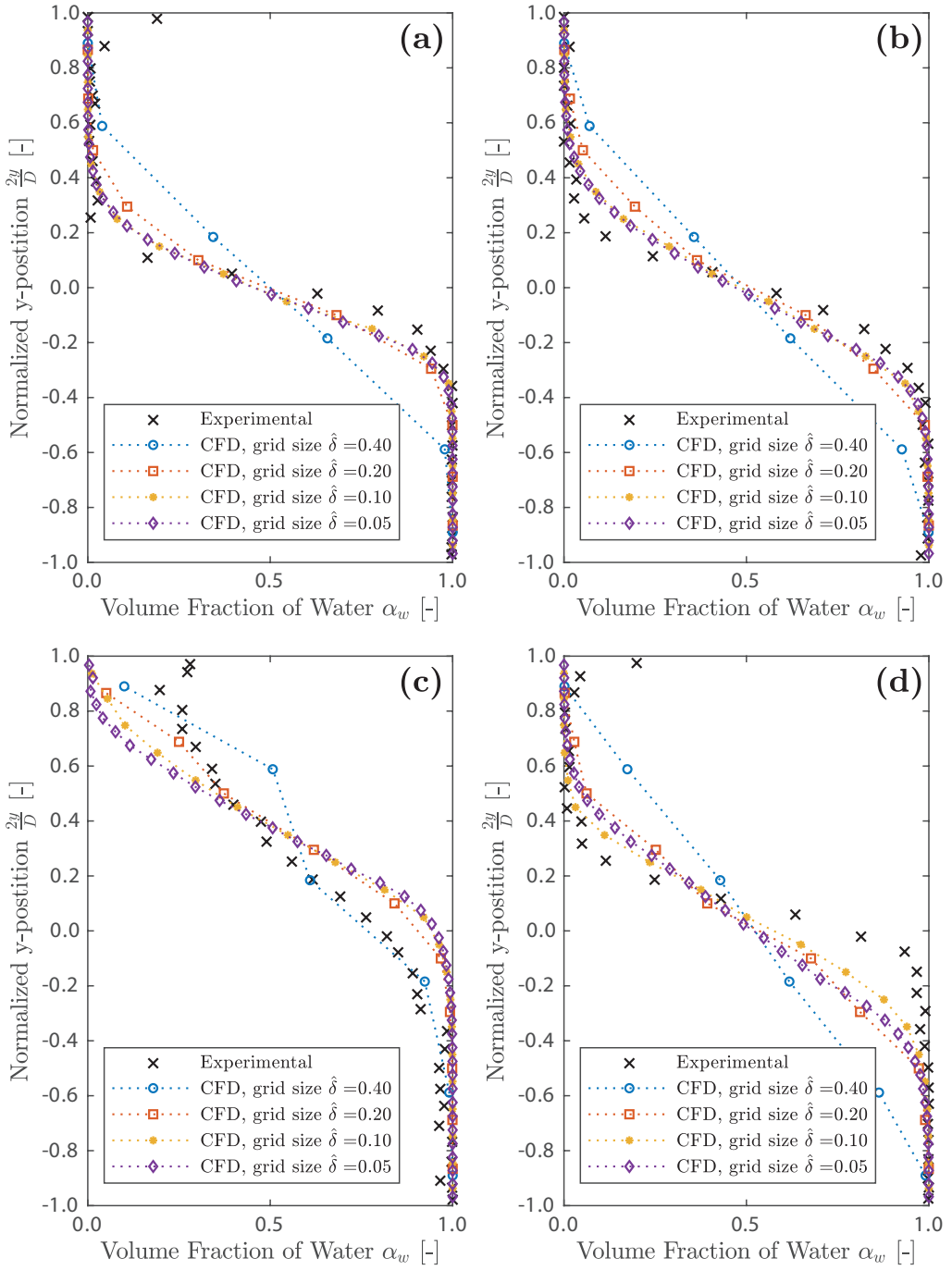

FIG. 6: Mesh convergence study showing cross-sectional volume fraction averages for four successively decrementing grid sizes: (a) horizontal flow, $U = 1.0$ m/s, $\psi = 50\%$; (b) horizontal flow, $U = 1.5$ m/s, $\psi = 50\%$; (c) horizontal flow, $U = 1.5$ m/s, $\psi = 75\%$; and (d) $\beta = 5^\circ$ upward inclined flow, $U = 1.0$ m/s, $\psi = 50\%$. Experimental reference by Kumara et al. (2009).

Near the bottom and top of the pipe ($2y/D = -1$ and $2y/D = 1$), the experimental results are not accurate and the deviations ignored (Kumara et al., 2009). Observed deviations in the experimental data suggest that the deviations lie within the expected uncertainty.

With increasing flow velocity, the phases disperse more. Similarly to the slower flow, the simulation run at $U = 1.5$ m/s mean velocity shown in Fig. 6(b) yields convergence toward a result slightly more dispersed than the experimental. On the contrary, at $\psi = 75\%$ water-cut, as shown in Fig. 6(c) the model does not seem to converge within the mesh sizes and seems to under-predict the level of dispersion.

As the pipe is inclined, transition to a wavy flow is expected where the time average would yield higher dispersion. For the upward inclined flow at 5 deg [Fig. 6(d)] similar convergence as for the horizontal flows is observed. Notably, the phase distribution profiles converges at around $\hat{\delta} = 0.1$ for all the cases.

3.3 Droplet Size Comparison

The droplet size distribution resulting from the S-gamma model is visually shown in Fig. 7 and compared to droplets visually observed during experimental work by Elseth (2001) in Table 3. The modeled droplet sizes were sampled over a five-diameter test section and maximums taken. As the modeled droplets were the Sauter mean diameter, they are divided by 0.48 to compare

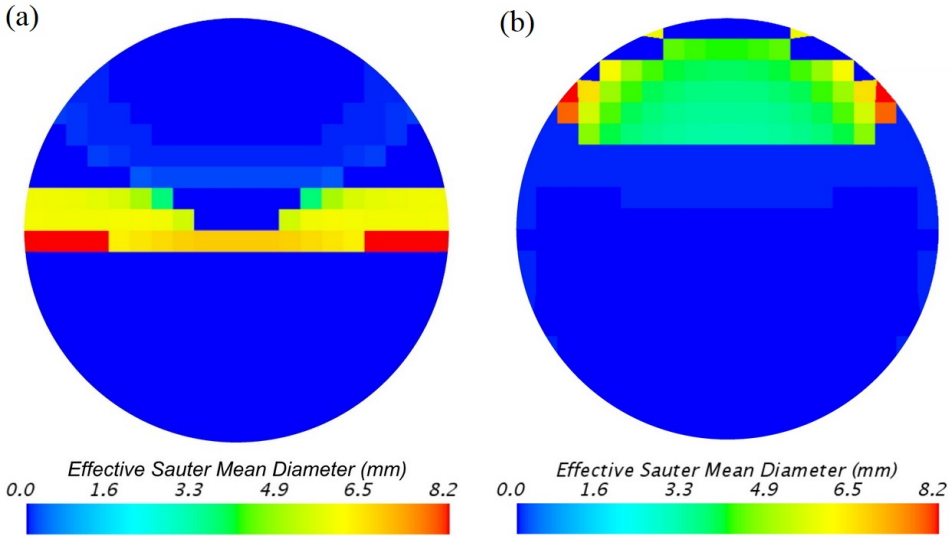

FIG. 7: Cross-sectional droplet Sauter mean diameters d_{32} at $x = 55D$ and horizontal flow, $U = 1.0$ m/s, and (a) $\psi = 50\%$ and (b) $\psi = 75\%$

TABLE 3: Comparison between the experimentally observed droplet sizes from Elseth (2001) and the CFD results taken at $x = 55D$ as well as the empirical correlations from Brauner (2001)

β (deg)	U (m/s)	ψ (%)	Exp. (mm)	CFD (mm)	Emp. (mm)
0	1.0	50	3	12.8	11
0	1.0	75	8	8.1	9

to maximum observed droplet sizes, as described in Eq. (27). From the results, it is seen that the S-gamma model predicts a droplet size consistent with the empirical correlation but seems to overestimate droplet sizes compared to the experimental observations. This could be due to limitations in the breakup and coalescence models or inaccurate model parameters.

3.4 Water-Wetting, Liquid Holdup and Dispersion

A study is performed on quantification of water-wetting along with an estimation of liquid holdup and dispersion with variations in the Froude, Richardson, and Atwood numbers. For this study, a grid size of $\hat{\delta} = 0.1$ is used and the analysis data are extracted from a pipe section between $x = 55D$ and $x = 60D$. The models are run at $\beta = 5^\circ$ inclination with $U = 1.0$ m/s mean velocity and $\psi = 50\%$ water-cut.

The effect of the Froude number is simulated using three different gravitational constants, thereby keeping all other flow parameters constant. The resulting variations of the liquid holdup and water wetting are listed in Table 4. It is seen that the liquid holdup decreases for increasing Froude numbers as the effect of difference in densities is reduced. At the same time, the water-wetting increases slightly. This can be described by a higher dispersion. This is shown in the density-plot in Fig. 8(a), where it is seen that the rate of dispersion increases with the Froude number.

The density difference characterized through the Atwood number is analyzed while keeping the mean density and thus the rest of the flow properties constant. The results are listed in Table 5 and shown as cross-sectional density plots in Fig. 8(b). Here, the increase of the Atwood number shows a larger liquid holdup with a lower dispersion. The water-wetting remains roughly constant.

4. CONCLUSIONS

The present study has employed a CFD model to capture the flow patterns and phase distribution in a two-phase oil and water flow. The model has been refined and validated against experimental data with mean flow velocity of $U = 1.0$ and $U = 1.5$ m/s and water-cuts $\psi = 50$ and $\psi = 75\%$. Here, the model shows good convergence and agreement with the experimental data in terms of phase distribution. The S-gamma model produces droplet sizes in good agreement with empirical correlations but overpredicts compared to those observed in experiments. This suggests that more work is necessary for an accurate prediction of the droplet size distribution. The physics causing the phase distribution are decomposed into dispersion and liquid holdup. This is used to analyze surface wetting for a set of Atwood and Froude numbers. The results show how the Atwood number balances dispersion to liquid holdup having a rather constant water-wetting; whereas, the water-wetting increases with the Froude number, although the liquid holdup is reduced. Both the Atwood number and the Froude number affect the Richardson number. It is clear that an

TABLE 4: Variation of the Froude number and the resulting Richardson number; mean velocity $U = 1.0$ m/s, inclination $\beta = 5$ deg, Re = 38,000, A = 0.12, and We = 1200

Fr	Ri	ψ (%)	Liquid holdup (%)	Water-wetting (%)
1.0	0.51	50	53.5	54.1
1.3	0.26	50	51.4	54.0
1.9	0.13	50	51.0	55.1

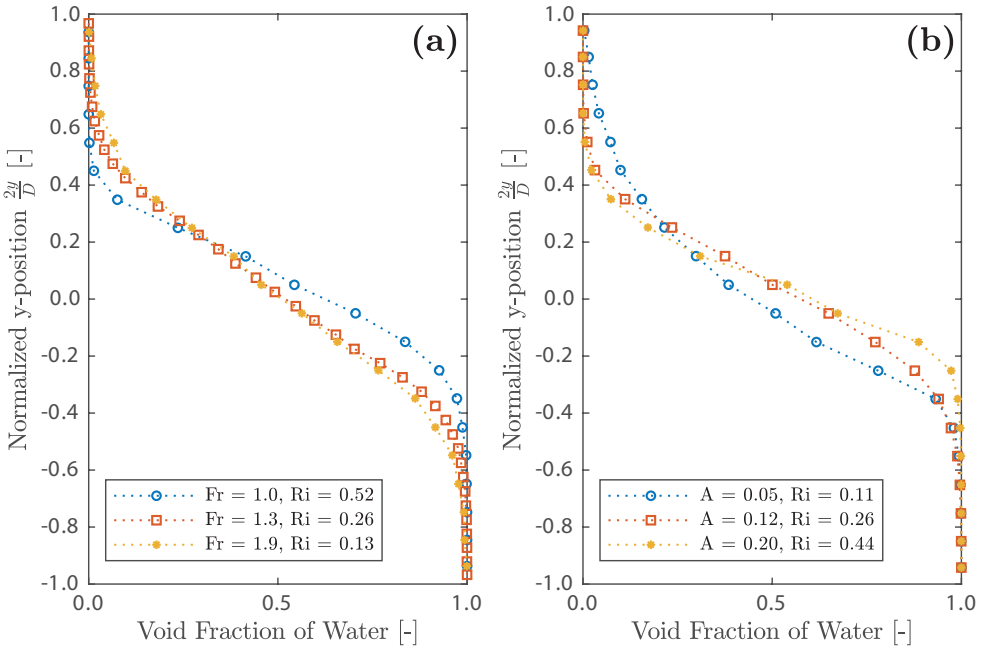

FIG. 8: Cross-sectional density plots at $U = 1.0$ m/s, $\psi = 50\%$, $\beta = 5$ deg, Re = 38,000, We = 1200: (a) variation of the Froude number at A = 0.12 and (b) variation of the Atwood number at Fr = 1.3

TABLE 5: Variation of the Atwood number and the resulting Richardson number; mean velocity $U = 1.0$ m/s, inclination $\beta = 5$ deg, Re = 38,000, Fr = 1.3, and We = 1200

A	Ri	ψ (%)	Liquid holdup (%)	Water-wetting (%)
0.05	0.11	50	50.3	55.2
0.12	0.26	50	51.4	54.0
0.20	0.44	50	54.0	54.7

increased Richardson number stabilizes the flow as expected from the relation to the Kelvin-Helmholtz instability.

REFERENCES

Angeli, P. and Hewitt, G.F., Drop Size Distributions in Horizontal Oil-Water Dispersed Flows, *Chem. Eng. Sci.*, vol. **55**, no. 16, pp. 3133–3143, 2000.

Auton, T.R., Hunt, J.C.R., and Prud'Homme, M., The Force Exerted on a Body in Inviscid Unsteady Non-Uniform Rotational Flow, *J. Fluid Mech.*, vol. **197**, pp. 241–256, 1988.

Brackbill, J.U., Kothe, D.B., and Zemach, C., A Continuum Method for Modeling Surface Tension, *J. Comput. Phys.*, vol. **100**, no. 2, pp. 335–354, 1992.

Brauner, N., The Prediction of Dispersed Flows Boundaries in Liquid-Liquid and Gas-Liquid Systems, *Int. J. Multiphase Flow*, vol. **27**, no. 5, pp. 885–910, 2001.

Cerne, G., Petelin, S., and Tiselj, I., Coupling of the Interface Tracking and the Two-Fluid Models for the Simulation of Incompressible Two-Phase Flow, *J. Comput. Phys.*, vol. **171**, pp. 776–804, 2001.

Coste, P., A Large Interface Model for Two-Phase CFD, *Nucl. Eng. Des.*, vol. **255**, pp. 38–50, 2013.

dos Santos, R.G., Mohamed, R.S., Bannwart, A.C., and Loh, W., Contact Angle Measurements and Wetting behavior of Inner Surfaces of Pipelines Exposed to Heavy Crude Oil and Water, *J. Pet. Sci. Eng.*, vol. **51**, pp. 9–16, 2006.

Drazin, P.G. and Reid, W.H., *Hydrodynamic Stability*, 2nd Ed., Cambridge, UK: Cambridge University Press, 2004.

Elseth, G., An Experimental Study of Oil/Water Flow in Horizontal Pipes, PhD, Telemark University College, 2001.

Glimm, J., Grove, J.W., Li, X.L., Oh, W., and Sharp, D.H., A Critical Analysis of Rayleigh-Taylor Growth Rates, *J. Comput. Phys.*, vol. **169**, no. 2, pp. 652–677, 2001.

Goldstein, S., On the Stability of Superposed Streams of Fluids of Different Densities, *Proc. R. Soc. A*, vol. **132**, no. 820, pp. 524–548, 1931.

Hazel, P., Numerical Studies of the Stability of Inviscid Stratified Shear Flows, *J. Fluid Mech.*, vol. **51**, no. 1, pp. 39–61, 1972.

Hill, D.P., An Experimental Study of Oil/Water Flow in Horizontal Pipes, PhD, University of London, 1998.

Hirt, C.W. and Nichols, B.D., Volume of Fluid (VOF) Method for the Dynamics of Free Boundaries, *J. Comput. Phys.*, vol. **39**, no. 1, pp. 201–225, 1981.

Ishii, M. and Hibiki, T., *Thermo-Fluid Dynamics of Two-Phase Flow*, 2nd Ed., New York: Springer, 2006.

Kumara, W.A.S., Elseth, G., Halvorsen, B.M., and Melaaen, M.C., Computational Study of Stratified Two Phase Oil/Water Flow in Horizontal Pipes, *HEFAT 2008*, Citeseer, 2008.

Kumara, W.A.S., Halvorsen, B.M., and Melaaen, M.C., Pressure Drop, Flow Pattern and Local Water Volume Fraction Measurements of Oil-Water Flow in Pipes, *Meas. Sci. Technol.*, vol. **20**, p. 114004, 2009.

Lamb, S.H., *Hydrodynamics*, 6th Ed., New York: Dover Publications, 1932.

Lance, M. and Bataille, J., Turbulence in the Liquid-Phase of a Uniform Bubbly Air Water-Flow, *J. Fluid Mech.*, vol. **222**, pp. 95–118, 1991.

Lo, S. and Zhang, D., Modelling of Break-Up and Coalescence in Bubbly Two-Phase Flows, *Int. Comm. Heat Mass Transfer*, vol. **1**, no. 1, pp. 23–38, 2009.

Muzaferija, S. and Peric, M., Computation of Free Surface Flows Using Interface-Tracking and Interface-Capturing Methods, *Numer. Heat Transfer, Part B*, vol. **32**, no. 4, pp. 369–384, 1997.

Pouraria, H., Seo, J.K., and Paik, J.K., A Numerical Study on Water Wetting Associated with the Internal Corrosion of Oil Pipelines, *Ocean Eng.*, vol. **122**, pp. 105–117, 2016.

Prosperetti, A. and Tryggvason, G., *Computational Methods for Multiphase Flow*, Cambridge, UK: Cambridge University Press, 2007.

Schiller, L. and Naumann, A., Über Die Grundlegende Berechnungen Bei Der Schwerkraftaufbreitung, *Z. Ver. Deutsch. Ing.*, vol. **77**, no. 12, pp. 318–320, 1933.

Schümann, H., Khatibi, M., Tutkun, M., Pettersen, B.H., Yang, Z., and Nydal, I.J., Droplet Size Measurements in Oil-Water Dispersions: A Comparison Study Using FBRM and PVM, *J. Disp. Sci. Tech.*, vol. **36**, no. 10, pp. 1432–1443, 2015.

Shih, T., Liou, W.W., Shabbir, A., Yang, Z., and Zhu, J., A New k-ϵ Eddy Viscosity Model for High Reynolds Number Turbulent Flows, *Comput. Fluids*, vol. **24**, no. 3, pp. 227–238, 1995.

Strubelj, L., Tiselj, I., and Mavko, B., Simulations of Free Surface Flows with Implementation of Surface Tension and Interface Sharpening in the Two-Fluid Model, *Int. J. Heat Fluid Flow*, vol. **30**, no. 4, pp. 741–750, 2009.

Taylor, G.I., Effect of Variation in Density on the Stability of Superposed Streams of Fluid, *Proc. R. Soc. A*, vol. **132**, no. 820, pp. 499–523, 1931.

Taylor, G.T., The Instability of Liquid Surfaces when Accelerated in a Direction Perpendicuar to Their Planes, *Proc. R. Soc. Lond.*, vol. **201**, pp. 192–196, 1950.

Turner, J.S., *Buoyancy Effects in Fluids*, Cambridge, UK: Cambridge University Press, 1973.